The Effect of Insulating Layers on the Performance of Implanted Antennas

Francesco Merli, *Student Member, IEEE*, Benjamin Fuchs, *Member, IEEE*, Juan R. Mosig, *Fellow, IEEE*, and Anja K. Skrivervik

***Abstract*—This work presents the analysis of the influence of insulation on implanted antennas for biotelemetry applications in the Medical Device Radiocommunications Service band. Our goal is finding the insulation properties that facilitate power transmission, thus enhancing the communication between the implanted antenna and an external receiver. For this purpose, it has been found that a simplified model of human tissues based on spherical geometries excited by ideal sources (electric dipole, magnetic dipole and Huygens source) provides reasonable accuracy while remaining very tractable due to its analytical formulation. Our results show that a proper choice of the biocompatible internal insulation material can improve the radiation efficiency of the implanted antenna (up to six times for the investigated cases). External insulation facilitates the electromagnetic transition from the biological tissue to the outer free space, reducing the power absorbed by the human body. Summarizing, this work gives insights on the enhancement of power transmission, obtained with the use of both internal, biocompatible and external, flexible insulations. Therefore, it provides useful information for the design of implanted antennas.**

***Index Terms*—Biocompatible antenna, implanted antennas, insulation, Medical Device Radiocommunications Service (MedRadio), spherical wave expansion.**

I. Introduction

NOWADAYS there is a growing interest in devices for implantable biotelemetry applications in the Medical Device Radiocommunications Service (MedRadio, 401–406 MHz) [1]. In order to improve the comfort of the patient, the whole system, including the antenna, must be as small as possible. This, along with the choice of the MedRadio band, (formerly Medical Implantable Communication Services band) implies the use of an electrically small antenna [2]–[8].

Such antennas are very sensitive to their surrounding environment. The properties of implanted antennas (resonance frequency, bandwidth, efficiency, etc.) are indeed strongly affected by the presence of the human body. So as to predict these modifications, many 'body phantoms' have been developed and are available in [9] (and references therein) and [10]–[13]. These models describe the human body with different accuracy (in terms of geometry, number of tissues and voxel precision). Particular attention is paid to the fact that the human body is constituted of highly lossy materials for RF propagation, for instance $\tan\delta = 0.6219$ at 403.5 MHz for muscle tissue [14]. Communication between the implanted antenna and the external base station is significantly affected. Hence, it is necessary to evaluate the power absorbed by the human tissues, both to predict the power link budget and to fulfill safety compliance [15].

Antennas immersed in lossy media have been deeply investigated for submarine and subsurface systems (for instance in [16]). Then, spherical multilayered models have been considered for various applications, including biomedical ones. It turns out that, although being a rough approximation of the human body, such multishell models are very useful [2], [17]–[21].

In this paper, the spherical model is first enriched with the presence of a realistic biocompatible insulation in proximity of the excitation as shown in Fig. 1. This material plays an important role for the mechanical, biological and electromagnetic properties of any implanted device. For instance, the biocompatible insulation is necessary to prevent metallic oxidation and to avoid any short-circuit effect due to the high conductivity of some human body tissues. In particular, the biocompatible insulation affects the electromagnetic radiation in different physical ways: it smooths the transition of the radiating wave between the source and the body model (this facilitates the radiation and increases the efficiency); it also reduces the coupling (i.e., dissipation) of the high near field terms of the electromagnetic radiation in the surrounding living tissue. The latter plays a principal role in the radiation efficiency of the implanted antenna.

This work focuses on the power transmission enhancement that can be obtained with an internal insulation from an implanted source, as introduced in [3]–[6], [16], [22]. In particular, results regarding the effect of insulation layers on real sources are reported in [3]–[5].

Three distinct superstrates, that do no completely surround the source and have different thicknesses and ε_r' (varying within 3 and 9), are considered in [3], while [4] presents only thickness variation and [5] emphasizes the impact of coating thickness over time. As clearly pointed out in these works, varying the insulation properties strongly modifies the radiation characteristics and hence the input impedances, matching and efficiencies. Radiation efficiencies at different resonant frequencies and/or matching levels are compared in [3]–[5]. Theoretical results on the broad band matching properties achievable by insulated implanted antennas are presented in [6], supported by a practical realization. Finally, a prominent study has been reported in [16], where the theoretical and numerical analysis

Manuscript received November 05, 2009; revised July 21, 2010; accepted October 13, 2010. Date of publication November 01, 2010; date of current version January 04, 2011. This work was supported in part by COST IC0603 Antenna Systems & Sensors for Information Technologies Society (ASSIST).

F. Merli, J. R. Mosig, and A. K. Skrivervik are with the Laboratoire d'Electromagnétisme et d'Acoustique (LEMA), Ecole Polytechnique Fédérale de Lausanne (EPFL), Lausanne CH-1015, Switzerland (e-mail: francesco.merli@epfl.ch).

B. Fuchs is with the Institute of Electronics and Telecommunications of Rennes, UMR CNRS 6164, University of Rennes I, Rennes Cedex 35042, France (e-mail: benjamin.fuchs@univ-rennes1.fr).

Color versions of one or more of the figures in this paper are available online at http://ieeexplore.ieee.org.

Digital Object Identifier 10.1109/TAP.2010.2090465

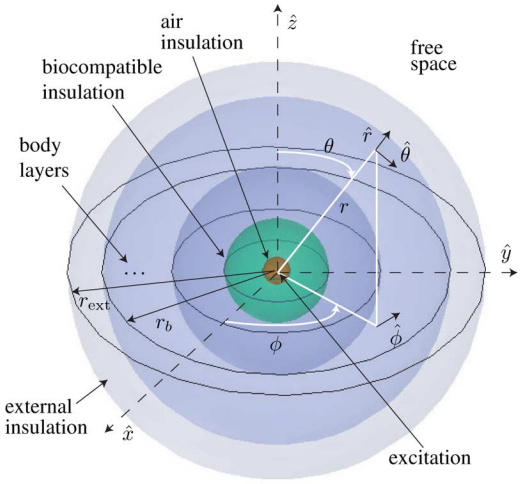

Fig. 1. Three-dimensional view of the analyzed structure with the notations and the spherical coordinate system. The excitation is placed at the center of several concentric spherical dielectric shells in the air. The spherical shells enable one to model the air, the biocompatible insulation, the body layers as well the external insulation.

discusses the effect of insulation on electromagnetic field and current distributions. Although this work is performed with a different modeling frame, our findings mostly match the conclusions of the aforementioned, as evidenced in Sections II–VI.

In this paper, the results shown in [22] are extended in order to give quantitative and qualitative insights on the effect of biocompatible materials in implanted antennas for telemetry applications. Both internal and external insulations are considered providing useful guidelines for the design of implanted antenna. Note that although the results are presented in MedRadio band, the numerical analysis can be straightforwardly extended to any other working frequency.

This paper is organized as follows: Section II describes the properties (geometrical and electrical) of the investigated models as well as the analytical method, based on the spherical wave expansion, used to solve the electromagnetic problem. The numerical implementation of the code is discussed in Section III and validated by comparisons with a commercial software [23]. Section IV presents the obtained numerical results. In Section V, the model takes into account the presence of an external insulation layer, as depicted in Fig. 1. As the body model is a bounded lossy medium, the electromagnetic propagation between the body layer and the outside free space is investigated considering the presence of flexible insulations. Finally, conclusions are drawn in Section VI.

II. Modeling and Analysis

A. Human Body Model and Biocompatible Insulation Layer

A multilayered spherical model provides worthwhile results despite the rough approximation of the human body, as previously discussed in [2], [17]–[20]. It represents indeed a good *average* of more complex models. For instance, radiation efficiencies, specific absorption rate (SAR) and power profiles have been presented in [2], [18], [20] and [17], [21]. Obviously, depending on the source modeling, unrealistically high values of the absolute electric field (therefore SAR) can be obtained

TABLE I
Geometrical and Electrical Description of the Analyzed Body Models

	Model	Dielectric properties		Radius
		$\varepsilon_r' - j\varepsilon_r''$	$\tan\delta$	[mm]
1	IEEE head model [15, p. 36]	43.50 - j 34.75	0.7989	90
2	Muscle tissue	57.10 - j 35.51	0.6219	90
3	Muscle tissue	57.10 - j 35.51	0.6219	82
	Fat tissue	5.58 - j 1.83	0.3280	86
	Dry skin tissue	46.70 - j 30.72	0.6578	90

[24]. Nevertheless, even for SAR investigation, relative differences and tendencies are still correctly predicted, and this is very useful for the comprehension of the effects of biocompatible insulations. Hence this work, that mainly focuses on the effect of biocompatible insulation on radiation efficiency, considers and analyzes spherical body phantoms.

The model, represented in Fig. 1, is composed of several concentric spherical shells whose dielectric properties are similar to those of real human tissues (values taken from [14]). Three body models, two homogeneous and one multilayered, are investigated. Table I reports the geometrical (shell radii) and physical description (dielectric properties) of the different body phantoms. The radii of the equivalent human tissues are set being inspired by [2]. The selected models are representative of the overall obtained results.

The insulation layer is modeled as a homogeneous spherical shell whose dielectric properties are the same as real biocompatible materials. Since a discussion on biomaterials is out of the scope of this work, standard biocompatible insulations have been taken from [25] and [26]. For our application, that requires electromagnetic power transmission, high conductivity materials (such as gold or silver) are not appropriate. Thus, three polymers (polypropylene, peek and polyamide) and two ceramics (alumina and zirconia) have been selected as representative of the acceptable possibilities.

Note that for physical reasons, detailed in Section II-D, excitation is first insulated by an air shell, in turn surrounded by biocompatible material, as shown in Fig. 1.

B. Electromagnetic Analysis Method

This Section sets the mathematical notations and describes how to compute the electromagnetic field. The following standard development, although well known from classical works [27] is summarized here for the sake of completeness and for a better understanding of Sections III–VI.

In order to match the geometry of the analyzed structure shown in Fig. 1, the spherical coordinate system is used. Time harmonic dependence e^{jwt} is omitted for clarity. The electromagnetic field $(\vec{E},\vec{H})$ is expanded on the spherical modal basis $\{\vec{M},\vec{N}\}$ as follows:

$$\begin{matrix}\vec{E}\\ -j\zeta\vec{H}\end{matrix} = \sum_{n,m,\sigma,s} a_{mn}^{\sigma s}\begin{matrix}\vec{M}_{mn}^{\sigma s}\\ \vec{N}_{mn}^{\sigma s}\end{matrix} + b_{mn}^{\sigma s}\begin{matrix}\vec{N}_{mn}^{\bar{\sigma} s}\\ \vec{M}_{mn}^{\bar{\sigma} s}\end{matrix}$$

$$\text{where } \sum_{n,m,\sigma,s} = \sum_{n=1}^{+\infty}\sum_{m=0}^{n}\sum_{s=1,4}\sum_{\sigma=e,o} \tag{1}$$

where a and b are the spherical modal coefficients and ζ is the intrinsic medium impedance. m and n are the mode indexes, $\sigma \in \{e, o\}$ and $\bar{\sigma}$ is its complement in the set.

The spherical wave vectors are

$$\begin{aligned} \vec{M}_{mn}^{\sigma s} &= \vec{\nabla} \times (\Psi_{mn}^{\sigma s} \vec{r}) \text{ and} \\ \vec{N}_{mn}^{\sigma s} &= \frac{1}{k} \vec{\nabla} \times \vec{\nabla} \times (\Psi_{mn}^{\sigma s} \vec{r}), \\ \text{with } \Psi(r, \theta, \varphi) &= Z_n^s(kr)\, P_n^m(\cos(\theta))\, f_m^\sigma(\varphi) \end{aligned} \tag{2}$$

where k is the intrinsic wave number. Z_n^1 and Z_n^4 are the spherical Bessel function of the first kind and Hankel function of the second kind, respectively. As for the azimuthal dependency, P_n^m stands for the associated Legendre polynomial of degree n and order m and $f_{o\,m}^{e}(\varphi) = \begin{matrix}\cos \\ \sin\end{matrix} m\varphi$.

A mode matching technique (MMT) based on spherical wave functions is used to compute the interaction between concentric spherical homogeneous layers and the selected source [28]. This method is well suited to analyze our problem since, a priori, there are no limitations regarding the dimensions and electromagnetic properties (permittivity, permeability and losses) of the layers. The MMT gives direct access to the field everywhere in a source free region, with controlled accuracy, as shown in Section III-A.

C. Power Computation

In presence of a lossy dielectric material of relative complex permittivity $\varepsilon_r = \varepsilon_r' - j\varepsilon_r''$, such as the human body, the available source power P_{source} is equal to

$$\begin{aligned} P_{\text{source}} &= P_{\text{rad}} + P_{\text{abs}} \\ &= \frac{1}{2} \oint_{S_r} \text{Re}(\vec{E} \times \overline{\vec{H}}) \cdot \hat{r} dS + \frac{\omega}{2} \int_V \varepsilon_0 \varepsilon_r' |\vec{E}|^2 dV \end{aligned} \tag{3}$$

where P_{rad} is the radiated power. P_{abs} represents the absorbed power related to both the near field ($1/r^2$, $1/r^3$ components) and far field ($1/r$ component). In fact, in a free space environment, the near-field is mainly reactive while, in our case, it strongly dissipates in the surrounding materials (insulation and body) increasing the loss of power [4], [16].

By substituting (1) and (2) into (3) and using the orthogonality properties of spherical modal vectors, given in Appendix A, one gets, after some manipulations, the analytical expression of the radiated power at any distance r

$$\begin{aligned} P_{\text{rad}}(r) = \frac{r^2}{2} \text{Re} \Bigg\{ \frac{j}{\bar{\zeta}} \sum_{n,m,\sigma,s} \cdots \\ \left(Z_n^s(z) \lambda_{mn}^\sigma \left(|a_{mn}^{\sigma s}|^2 \overline{K_n^s(z)} + a_{mn}^{\sigma s} \overline{a_{mn}^{\sigma \bar{s}}}\, \overline{K_n^{\bar{s}}(z)} \right) \right. \\ \left. + \overline{Z_n^s(z)} \lambda_{mn}^{\bar{\sigma}} \left(|b_{mn}^{\sigma s}|^2 K_n^s(z) + b_{mn}^{\sigma s} \overline{b_{mn}^{\sigma \bar{s}}}\, K_n^{\bar{s}}(z) \right) \right) \Bigg\} \end{aligned}$$

$$\text{where } \begin{cases} \lambda_{mn}^\sigma = \pi \frac{e_m^\sigma}{c_{mn}} \\ e_m^{\begin{matrix}e \\ o\end{matrix}} = 1 \pm \delta_m,\ \delta \text{ is the Krönecker symbol} \\ c_{mn} = \frac{2n+1}{2n(n+1)} \frac{(n-m)!}{(n+m)!} \\ K_n^s(z) = \frac{1}{z} \frac{d}{dz} (z Z_n^s(z)) \\ z = kr \end{cases} \tag{4}$$

in the above formulas ζ and k are the impedance and the wave number in the medium, respectively. Overlined symbols represent in general complex conjugate, save for $\bar{s}$ which means the complement in the set $\{1, 4\}$.

The net body loss, η_b, and the net insulation loss, η_{ins}, are defined as follows:

$$\begin{aligned} \eta_b &= -10 \log_{10} \frac{P_{\text{rad}}(r_b)}{P_{\text{rad}}(r_1)} \\ \eta_{\text{ins}} &= -10 \log_{10} \frac{P_{\text{rad}}(r_1)}{P_{\text{rad}}(r_0)} \end{aligned} \tag{5}$$

where r_b, r_1 and r_0 are the radii of the external body, the biocompatible insulation and the air shell, respectively. Consequently the total power attenuation, η_{tot}, due to the presence of the equivalent body model and the realistic internal insulation, is equal to $\eta_{\text{ins}} + \eta_b$.

The definition of the net body loss, η_b, is different from the one used in [10], [13] where $P_{\text{rad}}(r_b)$ is divided by the radiated power in free space. Our definition is not influenced by the dielectric loading of the surrounding tissue. Moreover, the power radiated by the source, $P_{\text{rad}}(r_0)$, is always normalized to 0 dBm.

D. Excitation

Ideal excitations are considered in this work. It is possible to model more realistic sources, as done in [2]. However, this leads to a significant increase of computation load which is not the goal of our work since we aim at providing some insights on the insulation layer influence.

The ideal source is placed at the origin of the concentric multishell body model in order to be surrounded by an insulation layer. Infinitesimal electric and magnetic dipoles are used. A Huygens source is also modeled. It consists of crossed electric and magnetic dipoles and it has the properties of radiating only in the forward direction [29]. It can therefore be considered as representative of some relatively directive antennas, with a preferred off-body direction of radiation.

As pointed out in [24], a Hertzian dipole radiating in an unbounded lossy medium must be supplied with infinite power, which is not physically meaningful. To overcome this problem, Tai suggested to insulate the dipole with a lossless sphere. This problem remains if the dipole is placed at the center of a bounded lossy layer (in this case spherical), as shown in Appendix B. Therefore it can be said that our acting source is a mathematical dipole source, surrounded and insulated by an air shell (Fig. 1).

III. Numerical Validation of the Method

A. Truncation Order

The series $\sum_n$ requires a truncation order N_t when numerically implemented. Many studies have discussed the choice of N_t in relation to the antenna size and with the focus on the far field accuracy (for instance [29], [30] and references therein). A convergence criterion, inspired by [30], is implemented to evaluate the relative amount of the truncated power $\xi_{P_{\text{tr}}}^{N_t}(r)$, at a given distance r including the near field ranges

$$\xi_{P_{\text{tr}}}^{N_t}(r) = \frac{P_{\text{rad}}^{N_t+1}(r) - P_{\text{rad}}^{N_t}(r)}{P_{\text{rad}}^{N_t}(r)}. \tag{6}$$

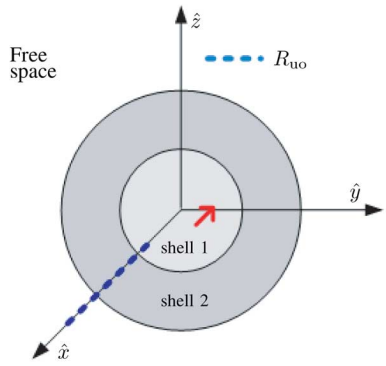

(a)

shell number	medium	radius r	complex rel. permittivity ε_r
1	air	5 mm $\simeq \frac{\lambda_o}{148}$	1.00
2	fat	8 mm $\simeq \frac{\lambda_o}{93}$	5.58 - j 1.83 [14]

(b)

Fig. 2. Description of the investigated electromagnetic problem for the numerical comparison with FEKO: (a) geometry and (b) environment properties (λ_o is the free space wavelength at 403.5 MHz). The Hertzian dipole, $\hat{\theta} = \pi/3$ and $\hat{\phi} = \pi/4$ oriented, is placed at $x = 1$, $y = 1$, $z = 1$ [mm].

In the above formula $P_{\rm rad}^{N_t}$ equals to $P_{\rm rad}$ in (4) replacing $\sum_n = \sum_{n=1}^{\infty}$ by $\sum_{n=1}^{N_t}$. The truncation order N_t is first set to be equal to $k_0 r_{\rm ext}$, where k_0 is the free space wave number and $r_{\rm ext}$ the radius of the biggest shell, as depicted in Fig. 1. N_t is then automatically increased until the neglected power $\xi_{P_{\rm tr}}^{N_t}(r)$ is below α

$$\max_{r \in R_{\rm uo}} \left\{ \xi_{P_{\rm tr}}^{N_t}(r) \right\} \leq \alpha, \tag{7}$$

where $R_{\rm uo}$ is the subset of the radial distances under observation.

B. Comparison With a Commercial Software

Let us consider the electromagnetic problem described in Fig. 2, where a Hertzian electric dipole is surrounded by two spherical shells. For the sake of comparison, small spherical shells radii are used.

The electric field is computed at 403.5 MHz and compared with the commercial code FEKO [23]. The MMT code and FEKO results are very close, as shown in Fig. 3. Logically, the agreement is better when $N_t = 21$ [Fig. 3(a)] than when $N_t = 11$ [Fig. 3(b)]. Slight discrepancies exist at the dielectric interfaces due to the mandatory FEKO's meshing of the spherical surfaces. In fact, for the computation of near field results, the commercial software applies the method of moments (MoM) in combination with the Surface Equivalence Principle (SEP). The latter calls for the meshing (with triangular basis function) of the surface of the spherical shells.

The relative amount of truncated power $\xi_{P_{\rm tr}}^{N_t}(r)$ is plotted on Fig. 4 for different values of N_t. As expected, the number of modes is critical when getting closer to the source. To reach $\xi_{P_{\rm tr}}^{N_t}(r) \leq \alpha = -140$ dB, $N_t = 21$ is thus required in shell number 1, whereas only 5 modes are sufficient from $r = 8$ mm (free space). For the far field description, $N_t = 1$ is enough. This

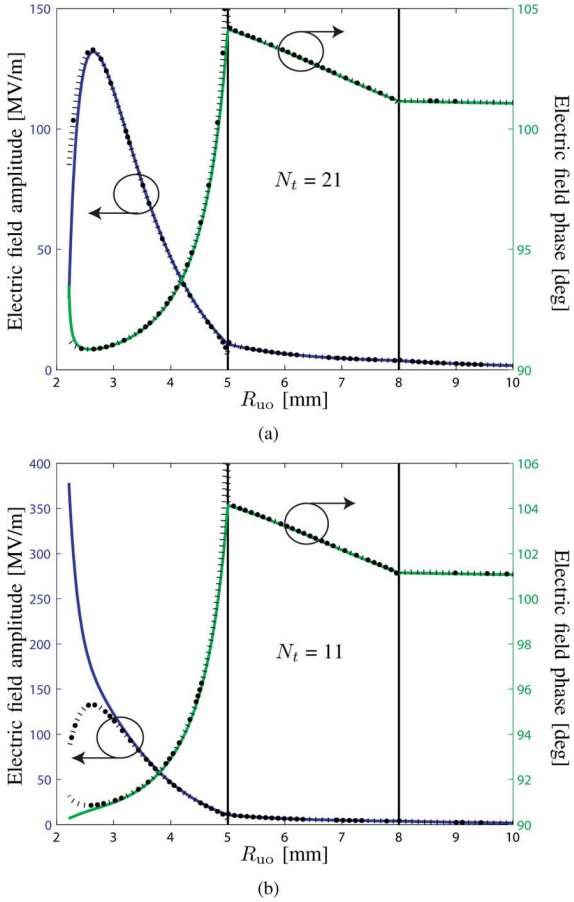

Fig. 3. Comparison of the $\hat{x}$ component of the electric field over $R_{\rm uo}$ (Fig. 2), between the MMT (solid line) code and FEKO (dotted line). Amplitude and phase are computed considering (a) $N_t = 21$ and (b) $N_t = 11$ which satisfy (7) for α equal to -140 and -70 dB, respectively. Vertical black lines indicate the shell boundaries.

is consistent with the classical recommendation $N_t = k_0 r_{\rm ext}$, as depicted in Fig. 5.

IV. Biocompatible Insulation: Numerical Results and Discussion

In this Section, we evaluate the effect of the internal biocompatible insulation. Three body models, described in Section II-A, are first analyzed in the presence of the electrical source. For the magnetic and the Huygens source, only the most relevant case is considered for the sake of clarity. The following characteristics are kept constant in the numerical analysis:

- working frequency of 403.5 MHz;
- the presence of 1 mm thick air insulation surrounding the excitation;
- the results are computed with a neglected power $\xi_{P_{\rm tr}}(r)$ lower than $\alpha = -140$ dB. This gives exact results over the desired $R_{\rm uo}$ as the source is placed at the origin.

Five different biocompatible materials, described in Table II, are investigated. Their thicknesses range from 1 to 4 mm. The computed net body, insulation and total losses (i.e., $\eta_{\rm ins}$, η_b and $\eta_{\rm tot}$, respectively) are reported in Tables III–V when the implanted antenna is insulated by the five biocompatible insulators. For a better understanding of the influence of the biocompatible materials, Tables III–V report even the no-insulation ("none") case.

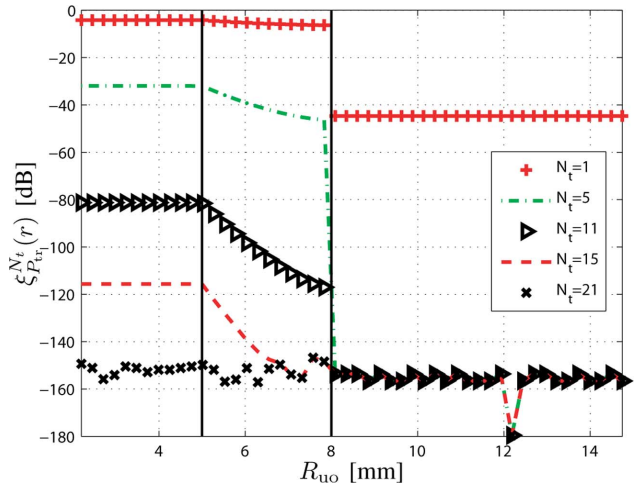

Fig. 4. Computation of the relative amount of truncated power, $\xi^{N_t}_{P_{\rm tr}}(r)$, over $R_{\rm uo}$ considering different values of N_t at 403.5 MHz for the problem described in Fig. 2.

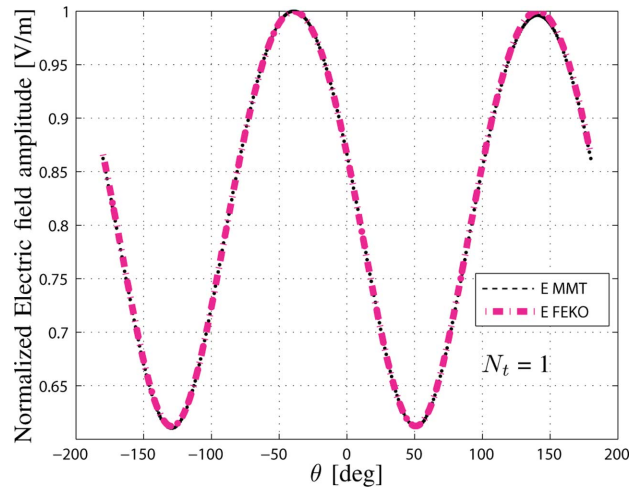

Fig. 5. Comparison between the MMT code and FEKO of the electric far field at 403.5 MHz considering $N_t = 1$ in the yz-plane for the problem described in Fig. 2.

This happens when the model has no biocompatible insulation layer, and it includes only the lossless air shell and the body equivalent spherical layers. Finally, it must be pointed out that (with the same working frequency, dielectric properties and loss definitions) our results are in the same order of magnitude than those presented in [10]–[13] (where more complex body models are considered).

A. Electrical Excitation

1) Model 1: IEEE Head Model: The use of the insulation layer strongly reduces the power dissipated in the body. Let us compare, in Table III, the η_b value of the none case (56.4 dB) with the results obtained by varying all the other insulators' thicknesses (i.e., 47.4, 42.2, 38.6 and 35.8 dB). A minimum improvement of 9 dB, and up to more than 20 dB, is found. Thus, the insulator is very useful to reduce the power absorbed by the body [3].

Consequently, the presence of the insulator reduces the total attenuated power $\eta_{\rm tot}$. With no insulation $\eta_{\rm tot} = 56.4$ dB

TABLE II
BIOCOMPATIBLE INTERNAL INSULATIONS

Material	Dielectric Properties	
	$\varepsilon'_r - j\varepsilon''_r$	$\tan\delta$
Polypropylene	2.55 - j 0.0076*	0.003
Peek	3.20 - j 0.0320*	0.010
Polyamide [31]	4.30 - j 0.0172	0.004
Alumina [31]	9.20 - j 0.0736	0.008
Zirconia (ZrO_2) [32]	29.0 - j 0.0507	0.002

* Measured values below 1 GHz.

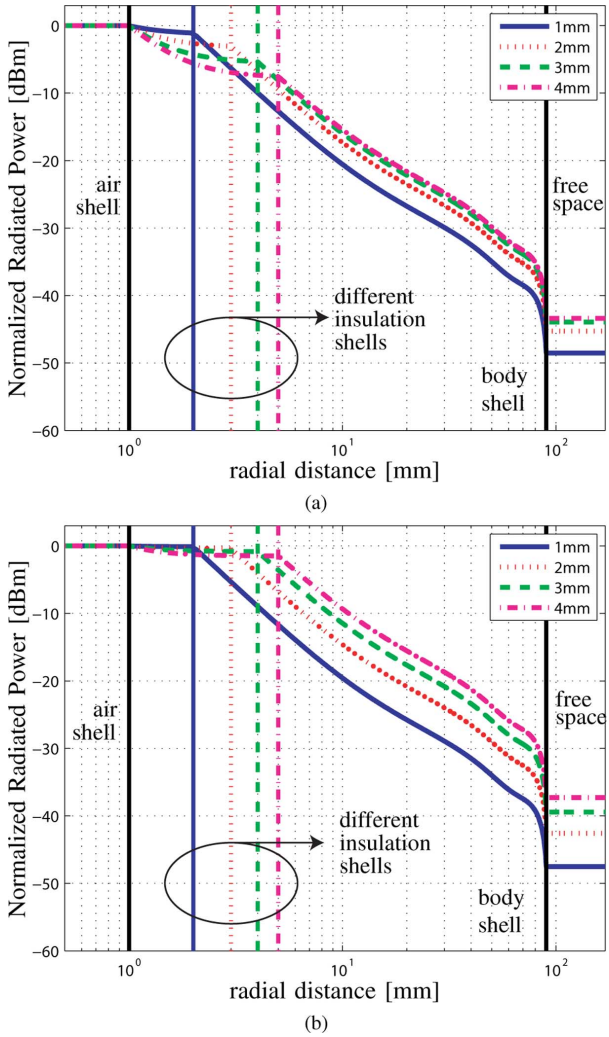

Fig. 6. Computation of $P_{\rm rad}$ as a function of the radial distance at 403.5 MHz for the IEEE homogeneous head model considering different (a) polypropylene and (b) zirconia insulation thicknesses.

whereas for all insulation materials and thicknesses, $\eta_{\rm tot}$ is lower than 50.3 dB. In particular the use of zirconia (4 mm thick) gives the best result with a 19 dB improvement (i.e., $56.4 - 37.3 = 19.1$ dB) while peek (1 mm thick) provides only a 6 dB increase (i.e., $56.4 - 50.3 = 6.1$ dB). This implies a remarkably larger efficiency (up to six times) for the implanted source.

Logically, and in agreement with [3], [4], [16], [33], increasing the thickness of the insulation reduces η_b and $\eta_{\rm tot}$.

TABLE III
POWER LOSS [DB] FOR DIFFERENT INTERNAL INSULATIONS WITH AN ELECTRIC DIPOLE IN MODEL 1 (IEEE HEAD MODEL)

Insulation	Thickness											
	1 mm			2 mm			3 mm			4 mm		
	$\eta_{\rm ins}$	η_b	$\eta_{\rm tot}$	$\eta_{\rm ins}$	η_b	$\eta_{\rm tot}$	$\eta_{\rm ins}$	η_b	$\eta_{\rm tot}$	$\eta_{\rm ins}$	η_b	$\eta_{\rm tot}$
Polypropylene	1.3		48.7	3.5		45.7	6.0		44.6	8.3		44.1
Peek	2.9		50.3	6.4		48.6	9.5		48.1	12.2		48.0
Polyamide	1.1	47.4	48.5	3.1	42.2	45.3	5.3	38.6	43.9	7.5	35.8	43.3
Alumina	1.1		48.5	3.0		45.2	5.3		43.9	7.5		43.3
Zirconia	0.1		47.5	0.4		42.6	0.8		39.4	1.5		37.3
none	$\eta_{\rm tot} = \eta_b = 56.4$											

TABLE IV
POWER LOSS [DB] FOR DIFFERENT INTERNAL INSULATIONS WITH AN ELECTRIC DIPOLE IN MODEL 2 (MUSCLE)

Insulation	Thickness											
	1 mm			2 mm			3 mm			4 mm		
	$\eta_{\rm ins}$	η_b	$\eta_{\rm tot}$	$\eta_{\rm ins}$	η_b	$\eta_{\rm tot}$	$\eta_{\rm ins}$	η_b	$\eta_{\rm tot}$	$\eta_{\rm ins}$	η_b	$\eta_{\rm tot}$
Polypropylene	1.8		46.7	4.4		44.1	7.1		43.2	9.5		42.9
Peek	3.7		48.6	7.6		47.3	10.9		47.0	13.5		46.9
Polyamide	1.5	44.9	46.4	3.9	39.7	43.6	6.4	36.1	42.5	8.7	33.4	42.1
Alumina	1.4		46.3	3.8		43.5	6.4		42.5	8.7		42.1
Zirconia	0.1		45.0	0.5		40.2	1.1		37.2	1.8		35.2
none	$\eta_{\rm tot} = \eta_b = 53.8$											

This behavior appears in Fig. 6, where the computed radiated power is higher when the insulation thickness increases. For instance, in the case of zirconia, η_b and $\eta_{\rm tot}$ with a 4 mm thick insulation layer are around 12 dB and 10 dB lower than when a thinner layer is used. However, this reduction highly depends on the insulation dielectric properties. There is indeed only a 2.3 dB reduction of $\eta_{\rm tot}$ when the peek thickness increases from 1 to 4 mm (i.e., $50.3 - 48.0 = 2.3\,\rm dB$) whereas 10.4 dB $(47.5 - 37.3 = 10.2\,\rm dB)$ are gained in the case of zirconia.

This result is very useful for the design of implanted antennas. In fact, as the volume of an implantable device is strictly limited, the radiator and the insulation dimensions have to be carefully chosen to optimize the radiation performances. Our values show that it is worth considering a thin peek insulation to allow the maximum volume for the antenna. On the contrary, in the case of zirconia, a relatively thicker insulation should be used. Moreover this dielectric material, due to its high ε_r', facilitates the reduction of the real antenna dimensions.

The use of zirconia gives always the best results for η_b and $\eta_{\rm tot}$. Clearly this material not only has the lowest $\tan\delta$, but also the ε_r' closest to the IEEE head model, thereby reducing the mismatch between the insulation and the body layer in agreement with [6]. On the other hand, peek presents the worst performances, as it shows the highest $\tan\delta$ and a low ε_r'.

Finally, the use of alumina or polyamide is almost equivalent (less than 0.1 dB variation) despite the fact that the $\tan\delta$ of this ceramic is double of the polyamide. This is again explained by the improved matching due to the higher ε_r' of the alumina.

2) Model 2: Muscle Model: All previous considerations, obtained with the IEEE head model, are still qualitatively confirmed in the muscle model, as reported in Table IV.

The dissipated powers in the muscle tissue, η_b, are smaller (of around 2.5 dB) as muscle presents a lower $\tan\delta$ than the IEEE head model (i.e., 0.6219 and 0.7989, respectively). On the contrary, the power attenuated in the insulation layer, $\eta_{\rm ins}$, is always higher (of around 1 dB). This is due to the mismatch between insulation and body model, which is more important in the case of the muscle since its permittivity ε_r' is higher than the one of IEEE head model (57.1 instead of 43.5).

This also implies that the choice of the biocompatible material has a deeper impact on the $\eta_{\rm ins}$ and, thus, on the total lost power $\eta_{\rm tot}$. For example, in the 1 mm case, we register a difference of 3.6 dB between peek and zirconia against the 2.8 dB value found in the IEEE head model. The same trend applies for all other thickness values.

3) Model 3: Multilayered Model: The results in Table V (multilayered model) are close to those in Table IV (muscle model). The first body shell surrounding the excitation is indeed the muscle in both models. The presence of the fat and dry skin layers changes the power losses ($\eta_{\rm ins}$, η_b and $\eta_{\rm tot}$) of less than 1 dB. This result is in agreement with [2], where the return losses of implanted antennas are very close when surrounded by these two body models.

B. Magnetic Excitation

The multilayered model with a 2 mm thick polyamide insulation is excited by a magnetic source. The choice of this insulation is justified as polymers are mechanically easier to manufacture and the polyamide has shown the best performances among them. Moreover, let us remind that polyamide presents performances very close to those of alumina, as shown in Section IV-A-I.

TABLE V
POWER LOSS [DB] FOR DIFFERENT INTERNAL INSULATIONS WITH AN ELECTRIC DIPOLE IN MODEL 3 (MULTILAYERED)

Insulation	Thickness											
	1 mm			2 mm			3 mm			4 mm		
	$\eta_{\rm ins}$	η_b	$\eta_{\rm tot}$	$\eta_{\rm ins}$	η_b	$\eta_{\rm tot}$	$\eta_{\rm ins}$	η_b	$\eta_{\rm tot}$	$\eta_{\rm ins}$	η_b	$\eta_{\rm tot}$
Polypropylene	1.8		45.8	4.4		43.3	7.1		42.4	9.5		42.1
Peek	3.7		47.7	7.5		46.4	10.8		46.1	13.5		46.1
Polyamide	1.5	44.0	45.5	3.8	38.9	42.7	6.4	35.3	41.7	8.7	32.6	41.3
Alumina	1.4		45.4	3.8		42.7	6.4		41.7	8.7		41.3
Zirconia	0.1		44.1	0.5		39.4	1.1		36.4	1.9		34.5
none	$\eta_{\rm tot} = \eta_b = 53.0$											

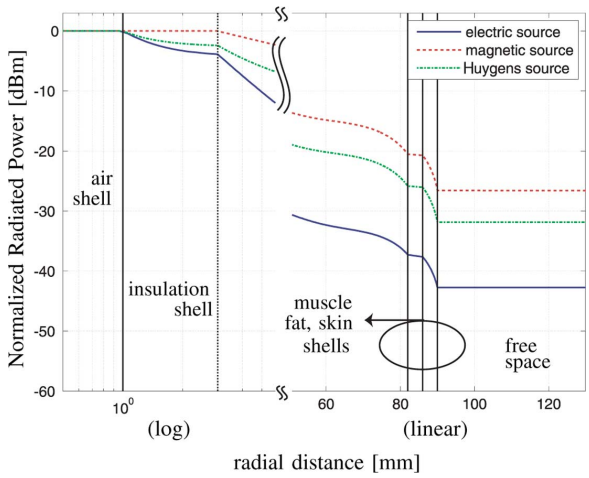

Fig. 7. Comparison of $P_{\rm rad}$ as a function of the radial distance at 403.5 MHz with the three different sources. The multilayered model is analyzed while considering the presence of polyamide 2 mm thick.

The power radiated through the body is compared in Fig. 7 for an electric and magnetic excitation. The magnetic source substantially reduces the absorbed power compared to the electric one ($\eta_{\rm ins} < 0.1$ dB and $\eta_b = \eta_{\rm tot} = 26.6$ dB instead of $\eta_{\rm ins} = 3.8$, $\eta_b = 38.9$ and $\eta_{\rm tot} = 42.7$ dB), for the same investigated model. The radiation of the magnetic source through a body is more efficient, as reported in [4], [22], [33]. The high magnetic near field does indeed not dissipate in the body since human tissues have no magnetic losses ($\mu_r'' = 0$). Finally, for a magnetic source, the dielectric characteristics of the real insulation layers have a negligible influence, as shown in [22].

C. Huygens Source

The power radiated through the body is computed for a Huygens source in the same conditions of the magnetic excitation. The level of the absorbed powers ($\eta_{\rm ins} = 2.4$, $\eta_b = 29.6$ and $\eta_{\rm tot} = 32$ dB) is between those of the electric and the magnetic excitation. Despite its 3 dB directivity, the radiation efficiency of the Huygens source is also between those of the electric and the magnetic dipoles. Indeed, it combines both sources. Therefore, the high electric near field coming from the electric dipole dissipates in the insulation and body layers, whereas the magnetic field is less affected.

TABLE VI
MAX SAR [DBW/KG] WITH DIFFERENT INTERNAL INSULATION THICKNESSES FOR THE MODELS OF SECTION IV

Insulation Thickness	Model 1 Elec.	Model 2 Elec.	Model 3 Elec.	Model 3 Magn.	Model 3 Huy.
none	40.7	40.6	40.7	24.4	36.8
1 mm	17.5	17.5	17.5	10.9	16.5
2 mm	12.2	12.2	12.2	5.4	10.2
3 mm	8.4	8.4	8.4	1.5	5.5
4 mm	5.4	5.4	5.4	-1.5	1.8

TABLE VII
FLEXIBLE EXTERNAL INSULATIONS

Material	Dielectric Properties	
	$\varepsilon_r' - j\varepsilon_r''$	$\tan\delta$
Fiber [38]	3.76 - j 0.0124	0.033
Neoprene [39]	6.50 - j 0.5850	0.090
Silicon (filled 67% TiO_2) [39]	8.50 - j 0.0085	0.001
ideal	7.9	0

The values reported in Tables III–V show, for a constant external diameter of the body shell, that the increase of the thickness of the insulation layer results in lower power dissipation in the living tissue. This conclusion holds true when different conditions for the body shell dimension are applied, such as constant volume [22] or thickness. In particular, the latter implies a slight increase of η_b of less than 0.2 dB.

D. Specific Absorption Rate

The maximum Specific Absorption Rate (SAR) values have been computed for the presented body models. It is well known that accurate and precise SAR values are strongly dependent on the human body representation, the implant locations and several biological phenomena [34]. Nevertheless, despite the simplicity of the investigated body models, it is worth evaluating the peak SAR values in order to confirm the observations previously reported.

Table VI reports the maximum values of SAR. These values are always found at the interface between the internal biocompatible layer and the human body. These peak values (with no spatial averaging) are obtained when the acting source (i.e., a mathematical dipole source surrounded by an air shell) radiates

TABLE VIII
POWER LOSS [DB] FOR DIFFERENT EXTERNAL INSULATIONS WITH THE HUYGENS SOURCE IN MODEL 3 (MULTILAYERED) AND A 2 MM THICK POLYAMIDE AS INTERNAL BIOCOMPATIBLE INSULATION

Insulation	Thickness								
	5 mm			10 mm			20 mm		
	η_b	$\eta_{\rm ext}$	$\eta_{\rm tot}$	η_b	$\eta_{\rm ext}$	$\eta_{\rm tot}$	η_b	$\eta_{\rm ext}$	$\eta_{\rm tot}$
Fiber	29.3	<0.1	31.7	29.1	<0.1	31.5	28.7	<0.1	31.1
Neoprene	29.2	0.3	31.9	29.0	0.5	31.9	28.3	0.8	31.5
Silicon	29.1	<0.1	31.5	28.8	<0.1	31.2	27.8	<0.1	30.2
ideal	η_b = 21.7 and $\eta_{\rm tot}$ = 24.1 ($\simeq$71 mm thick)								
none	η_b = 29.6 and $\eta_{\rm tot}$ = 32 dB								

0 dBm at the 1 mm air shell interface. The mass density values can be found in [2]. Of course, the use of such ideal sources provides unrealistically high values of the absolute electric field (therefore SAR) [24]. Thus, results are presented in [dB/W] so as better appreciate relative variations.

The presence of different insulation dielectric properties turns out to have a negligible effect on the obtained SAR values; therefore, only results versus the insulation thickness variation are reported. On the contrary, the relative peak SAR value variations with respect to the type of source and insulation thickness enables to derive valuable information, as reported below.

In agreement with the results already reported, the presence of any insulation produces a large impact reducing SAR values by at least 14 dB compared to the case without insulation (none). In the case of an electric source excitation a difference of approximately 12 dB is found versus the insulation thickness, which is in perfect agreement with the η_b values reported in Tables III–V.

As previously discussed, the magnetic source presence reduces the electric near field coupling in the biological tissue, consequently decreasing the SAR values with respect to the electrical excitation. The Huygens source case is relatively closer to the electric one. This is in agreement with the results reported graphically in Fig. 7.

As for the effect of the insulation thickness, an improvement of approximately 15 dB over the electric and magnetic cases (12 dB) is obtained in the presence of the Huygens source. Indeed, the increase of insulation thickness strongly reduces the coupling of the near field terms. Therefore, the far field component increases its relevance and the higher directivity inherent to the Huygens source plays a positive role since it reduces the SAR values.

V. EXTERNAL INSULATION: NUMERICAL RESULTS AND DISCUSSION

Our previous analysis clearly pointed out the importance of the biocompatible insulation layer. It is now logical to focus on the transition between the external body layer (skin) and the outer world (free space). The power transfer can be improved with the use of an insulation layer placed on the external surface of the human skin. For a practical wearable realization, one could imagine the use of an armband, belt or strap (for instance, as in tennis-elbow support).

The presence of an external layer has already been deeply investigated for many applications but, to the authors' best knowledge, not for implanted antennas for telemetry purposes in the MedRadio band. Among these applications, let us mention: SAR distribution and the microwave power coupling in hyperthermia [35], the electromagnetic absorption due to the presence of clothing (for instance [36]), the microwave coupling in medical imaging system [37] and SAR reduction from an undesired external source [38]. According to the application, the external insulator is called clothing, bolus, matching layer or shield. The major difference between these applications and our problem is that the source is always external to the body.

In this Section we focus on the power transmission enhancement that is achieved with the presence an the external insulator. A few types of materials are investigated. Those are: a polymer fiber, neoprene and silicon. Their dielectric properties are reported in Table VII, as well as the "ideal" case. The latter consists in the dielectric lossless shell that provides a perfect matching between the skin and the free space. The characteristics (permittivity and thickness) of this ideal matching layer are computed by analogy with the simple transmission line model [37]. This approximation is reasonable since only the far field term of the electromagnetic radiation is concerned, due to the electrically large distance between the source and the external layer.

External layers are modeled as spherical shells, whose thicknesses range from 5 to 20 mm, placed just after the body tissues, as shown in Fig. 1. For the numerical analysis, we consider the same characteristics listed in Section IV, with the Huygens source as the excitation, a 2 mm thick polyamide internal insulation and the multilayered body model.

The power attenuation in the internal 2 mm thick polyamide shell is $\eta_{\rm ins} = 2.4$ dB (as in Section IV-C). Table VIII reports the power attenuation in the multilayered model and the external insulation (η_b and $\eta_{\rm ext}$, respectively). Note that in this case $\eta_{\rm tot}$ is equal to $\eta_{\rm ins} + \eta_b + \eta_{\rm ext}$ with

$$\eta_{\rm ext} = -10 \log_{10} \frac{P_{\rm rad}(r_{\rm ext})}{P_{\rm rad}(r_b)} \tag{8}$$

where $r_{\rm ext}$ coincides with the radius of the external insulation shell (Fig. 1).

The cases of no external insulation ("none") and the lossless matching layer ("ideal") are also reported in Table VIII. The presence of the ideal insulation reduces $\eta_{\rm tot}$ of 7.9 dB compared to no insulation case ($29.6 - 21.7 = 7.9$ dB). This means establishing a communication almost three-times more efficient. Although not practically realistic (its thickness is approximately

71 mm) the ideal external insulation case is interesting to set the optimal value of the power transmission out of the skin tissue.

In agreement with [40], the presence of a thin external layer does not modify the η values as much as the internal biocompatible insulator. For instance, the power transmission is enhanced of almost 2 dB by the presence of a 20 mm thick silicon layer.

Although the investigated external insulations may not be the optimal ones, we have shown that their influence is not negligible.

VI. Conclusion

This work has analyzed the influence of insulation in implanted antennas for biotelemetry applications in the MedRadio band. Body models composed of concentric spherical homogeneous shells excited by ideal sources have been considered. The geometry of the structure allows to compute analytically the electromagnetic field with a Mode Matching Technique (MMT) based on spherical wave expansion. The MMT has been numerically validated by comparison with a full-wave commercial software. Moreover, a convergence criterion has been defined to compute, with controlled accuracy, the power radiated at any radial distance, including near field range.

Two homogeneous and one multilayered models have been investigated, considering both internal and external insulations.

The results obtained for the internal insulation provide guidelines, not only for the selection of the biocompatible material, but also for the implanted antenna design. In the strictly limited volume available for the implanted device, the dimensions of the antenna and insulation thickness must be carefully chosen so as optimize the radiation performances. For instance, a judicious choice of the internal biocompatible insulation leads up to a six-fold more efficient power transfer from the implanted source to the external receiver.

The influence of the type of excitation (electric and magnetic dipole and Huygens source) has also been examined. As expected, since the body does not present any magnetic loss, the magnetic source is the most efficient.

SAR values have been computed. Despite the limitations of the investigated body models, our results confirm the effective role of biocompatible internal insulation. Moreover, the important effect related to the near field coupling is once more emphasized by the Huygens source analysis.

The influence of external insulation has also been considered. An ideal matching layer, between the skin tissue and the air, increases the power transmission of almost 8 dB. The capability of a few low-loss, flexible materials has been analyzed to reduce the mismatch between the body layer and the outer free space. Although far from the ideal case, around 2 dB can be gained with realistic external insulators.

Despite the rough approximation of the human body and the use of ideal sources, the results presented above provide quantitative and qualitative insights on the power transmission enhancement that can be obtained with internal and external insulations. Moreover, presence of the insulation turns out to be an effective way to comply with SAR regulations.

Appendix A
Spherical Wave Properties

The spherical modal vectors $\vec{M}_{mn}^{\sigma s}$ and $\vec{N}_{mn}^{\sigma s}$ have several orthogonality properties. The one used to get the radiated power formula (4) are

$$\oint_{S_r} \begin{pmatrix} \vec{M}_{mn}^{\sigma s} \\ \vec{N}_{mn}^{\sigma s} \end{pmatrix} \times \overline{\begin{pmatrix} \vec{M}_{m'n'}^{\sigma' s'} \\ \vec{N}_{m'n'}^{\sigma' s'} \end{pmatrix}} \cdot \vec{dS} = 0 \tag{A-1}$$

and

$$\oint_{S_r} \left(\vec{M}_{mn}^{\sigma s} \times \overline{\vec{N}_{m'n'}^{\sigma' s'}} \right) \cdot \vec{dS} = \cdots \frac{\lambda_{mn}^{\sigma}}{|k|^2} |z|^2 Z_n^s(z) \overline{K_n^{s'}(z)} \delta_{\sigma,\sigma'} . \delta_{m,m'} . \delta_{n,n'}. \tag{A-2}$$

S_r is a sphere centered at the origin and $\delta_{p,q}$ is the Krönecker symbol.

Appendix B
Power Computation Considerations

A Hertzian dipole radiating in an unbounded lossy medium must be supplied with infinite power, which is not physically meaningful, as shown in [24]. This still applies for a dipole placed in a bounded lossy spherical shell. Equation (4) can be rewritten

$$P_{\mathrm{rad}}(r) = \frac{r^2}{2|\zeta|^2} \mathrm{Re} \left\{ j\zeta \sum_{n,m,\sigma,s} \gamma_{mn}^{\sigma s}(kr) \right\} \tag{B-1}$$

where ζ and k are complex values in a lossy shell. $\gamma_{mn}^{\sigma s}$ is a product of spherical modal coefficients and Bessel functions. If one lets r approach zero in (B-1), one can easily show that P_{rad} becomes infinite. One term of (B-1) is indeed proportional to $r^2 Z_n^4(kr) \overline{K_n^4(kr)}$ and this term has a $(kr)^{-(2n+1)}$ dependency when r tends toward zero, as shown in (B-2). The spherical Hankel functions Z_n^4 and K_n^4 have the following asymptotic behavior, given in [41, p. 437], as $|k|r \to 0$ and for $n = 1, 2, \ldots$

$$\begin{aligned} Z_n^4(kr) &\to \frac{1}{(2n+1)!!}(kr)^n + j(2n-1)!!(kr)^{-(n+1)}, \\ K_n^4(kr) &\to \frac{n+1}{(2n+1)!!}(kr)^{n-1} - jn(2n-1)!!(kr)^{-(n+2)}. \end{aligned} \tag{B-2}$$

This result confirms and extends, using the spherical modal expansion, the demonstration given in [24].

References

[1] Medical Device Radiocommunications Service (MedRadio) Medical Implanted Communication System (MICS), 2009 [Online]. Available: http://www.fcc.gov/

[2] J. Kim and Y. Rahmat-Samii, "Implanted antennas inside a human body: Simulations, designs, and characterizations," *IEEE Trans. Microwave Theory Tech.*, vol. 52, pp. 1934–1943, Aug. 2004.

[3] P. Soontornpipit, C. Furse, and Y. C. Chung, "Design of implantable microstrip antenna for communication with medical implants," *IEEE Trans. Microwave Theory Tech.*, vol. 52, pp. 1944–1951, Aug. 2004.

[4] P. S. Hall and Y. Hao, *Antennas and Propagation for Body-Centric Wireless Communications*. Norwood, MA: Artech House, 2006, ch. 9.

[5] R. Warty, M. R. Tofighi, U. Kawoos, and A. Rosen, "Characterization of implantable antennas for intracranial pressure monitoring: Reflection by and transmission through a scalp phantom," *IEEE Trans. Microwave Theory Tech.*, vol. 56, pp. 2366–2376, Oct. 2008.
[6] T. Dissanayake, K. P. Esselle, and M. R. Yuce, "Dielectric loaded impedance matching for wideband implanted antennas," *IEEE Trans. Microwave Theory Tech.*, vol. 57, pp. 2480–2487, Oct. 2009.
[7] S. Soora, K. Gosalia, M. S. Humayun, and G. Lazzi, "A comparison of two and three dimensional dipole antennas for an implantable retinal prosthesis," *IEEE Trans. Antennas Propag.*, vol. 56, pp. 622–629, Mar. 2008.
[8] T. Karacolak, R. Cooper, and E. Topsakal, "Electrical properties of rat skin and design of implantable antennas for medical wireless telemetry," *IEEE Trans. Antennas Propag.*, vol. 57, pp. 2806–2812, Sep. 2009.
[9] K. Ito, "Human body phantoms for evaluation of wearable and implantable antennas," presented at the 2nd Eur. Conf. on Antennas and Propagation (EuCAP 2007), Edinburgh, Scotland, UK, Nov. 2007.
[10] W. G. Scanlon, B. Burns, and N. E. Evans, "Radiowave propagation from a tissue-implanted source at 418 MHz and 916.5 MHz," *IEEE Trans. Biomed. Eng.*, vol. 47, pp. 527–534, Apr. 2000.
[11] L. C. Chirwa, P. A. Hammond, S. Roy, and D. R. S. Cumming, "Electromagnetic radiation from ingested sources in the human intestine between 150 MHz and 1.2 GHz," *IEEE Trans. Biomed. Eng.*, vol. 50, pp. 484–492, Apr. 2003.
[12] C. Miry, R. Gillard, and R. Loison, "An application of the multi-level dg-fdtd to the analysis of the transmission between a dipole in free-space and an implanted antenna in a simplified body model with various positions," in *Proc. 3rd Eur. Conf. on Antennas and Propagation EuCAP 2009*, Mar. 23–27, 2009, pp. 67–70.
[13] A. Sani, A. Alomainy, and Y. Hao, "Numerical characterization and link budget evaluation of wireless implants considering different digital human phantoms," *IEEE Trans. Microwave Theory Tech.*, vol. 57, pp. 2605–2613, Oct. 2009.
[14] C. Gabriel, Compilation of the Dielectric Properties of Body Tissues at RF and Microwave Frequencies Brooks Air Force Base, TX, 1996 [Online]. Available: http://niremf.ifac.cnr.it/tissprop/htmlclie/htmlclie.htm
[15] *Evaluating Compliance With FCC Guidelines for Human Exposure to Radiofrequency Electromagnetic Fields*, 97–01 ed. Washington, DC: Federal Communication Commission (FCC) Std. Supplement C, OET Bulletin 65, 2001.
[16] R. W. P. King and G. S. Smith, *Antennas in Matter: Fundamentals, Theory, and Applications*, 1st ed. Cambridge, MA: The MIT Press, 1981.
[17] C. M. Rappaport and F. R. Morgenthaler, "Optimal source distribution for hyperthermia at the center of a sphere of muscle tissue," *IEEE Trans. Microwave Theory Tech.*, vol. 35, pp. 1322–1327, Dec. 1987.
[18] K. S. Nikita, G. S. Stamatakos, N. K. Uzunoglu, and A. Karafotias, "Analysis of the interaction between a layered spherical human head model and a finite-length dipole," *IEEE Trans. Microwave Theory Tech.*, vol. 48, pp. 2003–2013, Nov. 2000.
[19] X.-K. K. L.-W. Li and M.-S. Leong, *Spheroidal Wave Functions in Electromagnetic Theory*, ser. Wiley Series in Microwave and Optical Engineering. New York: Wiley, 2002.
[20] S. M. S. Reyhani and S. A. Ludwig, "An implanted spherical head model exposed to electromagnetic fields at a mobile communication frequency," *IEEE Trans. Biomed. Eng.*, vol. 53, pp. 2092–2101, Oct. 2006.
[21] G. Cerri, R. De Leo, and G. Rosellini, "Evaluation of electromagnetic power deposition in a spherical multilayer head in the near field of a linear antenna," *Wireless Netw.*, vol. 3, pp. 499–510, 1997.
[22] F. Merli, B. Fuchs, and A. K. Skrivervik, "Influence of insulation for implanted antennas," in *Proc. 3rd Eur. Conf. on Antennas and Propagation EuCAP 2009*, Mar. 23–27, 2009, pp. 196–199.
[23] Feko Suite 5.3 (Evaluation Version, Silver License) [Online]. Available: http://www.feko.info/
[24] C. T. Tai and R. E. Collin, "Radiation of a Hertzian dipole immersed in a dissipative medium," *IEEE Trans. Antennas Propag.*, vol. 48, no. 10, pp. 1501–1506, Oct. 2000.
[25] Handbook of Materials for Medical Device ASM international, 2003, ch. 1.
[26] Zeus [Online]. Available: http://www.zeusinc.com/technicalservices/technicalbulletins/technicalinformation/biocompatibility.aspx
[27] J. A. Stratton, *Electromagnetic Theory*. New York: MGraw-Hill, 1941.
[28] B. Fuchs, S. Palud, L. L. Coq, O. Lafond, M. Himdi, and S. Rondineau, "Scattering of spherically and hemispherically stratified lenses fed by any real source," *IEEE Trans. Antennas Propag.*, vol. 56, no. 2, pp. 450–460, Feb. 2008.
[29] H. Mieras, "Radiation pattern computation of a spherical lens using mie series," *IEEE Trans. Antennas Propag.*, vol. 30, pp. 1221–1224, Nov. 1982.
[30] F. Jensen and A. Frandsen, "On the number of modes in spherical wave expansion," in *Proc. AMTA-2004*, Oct. 2004, pp. 489–494.
[31] Ansoft High Frequency Structure Simulator (HFSS) v11.1 (2009), Material Library [Online]. Available: http://www.ansoft.com/products/hf/hfss/
[32] T. Konaka, M. Sato, H. Asano, and S. Kubo, "Relative permittivity and dielectric loss tangent of substrate materials for high-tc superconducting film," *J. Supercond.*, vol. 4, no. 4, pp. 283–288, Aug. 1991.
[33] A. Karlsson, "Physical limitations of antennas in a lossy medium," *IEEE Trans. Antennas Propag.*, vol. 52, no. 8, pp. 2027–2033, Aug. 2004.
[34] P. R. Wainwright, "The relationship of temperature rise to specific absorption rate and current in the human leg for exposure to electromagnetic radiation in the high frequency band," *Phys. Med. Biol.*, vol. 48, no. 19, pp. 3143–3155, Oct. 2003.
[35] P. R. Stauffer, F. Rossetto, M. Leencini, and G. B. Gentilli, "Radiation patterns of dual concentric conductor microstrip antennas for superficial hyperthermia," *IEEE Trans. Biomed. Eng.*, vol. 45, pp. 605–613, May 1998.
[36] O. P. Gandhi and A. Riazi, "Absorption of millimeter waves by human beings and its biological implications," *IEEE Trans. Microwave Theory Tech.*, vol. 34, pp. 228–235, Feb. 1986.
[37] C. Rappaport, "Determination of bolus dielectric constant for optimum coupling of microwaves through skin for breast cancer imaging," *Int. J. Antennas Propag.*, p. 5, 2008, Article ID 359582.
[38] H.-Y. Chen and K.-Y. Shen, "Reduction of SAR in a human-head model wrapped in clothing materials," *Microwave Opt. Technol. Lett.*, vol. 37, no. 4, pp. 305–308, 2003.
[39] Tables of Physical and Chemical Constants Section 2.6.5 Kaye & Laby [Online]. Available: http://www.kayelaby.npl.co.uk/toc/
[40] H. Massoudi, C. H. Durney, P. W. Barber, and M. F. Iskander, "Electromagnetic absorption in multilayered cylindrical models of man," *IEEE Trans. Microwave Theory Tech.*, vol. 27, pp. 825–830, Oct. 1979.
[41] M. Abramowitz and I. A. Stegun, *Handbook of Mathematical Functions*. New York: Dover, 1965.

Francesco Merli (S'09) received the Laurea degree (*cum laude*) in telecommunication engineering from the University of Florence, Florence, Italy, in 2006. He is currently working towards the Ph.D. degree at Ecole Polytechnique Fédérale de Lausanne (EPFL).

His research interests include analysis, design and realization of implantable, small and UWB antennas.

Benjamin Fuchs (S'06–M'08) received both the electronics engineering degree and the M.S. degree in electronics from the National Institute of Applied Science (INSA), Rennes, France, in 2004 and the Ph.D. degree from the University of Rennes 1, France, in 2007.

In 2008, he was a Postdoctoral Research Fellow at the Swiss Federal Institute of Technology, Lausanne, Switzerland. In 2009, he joined the Institute of Electronics and Telecommunications of Rennes (IETR), as a Researcher at the Centre National de la Recherche Scientifique (CNRS). His research interests include mode matching techniques, millimeter-wave antennas, focusing devices (lens antennas) and beamforming.

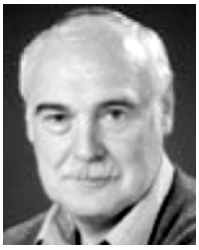

Juan R. Mosig (S'76–M'87–SM'94–F'99) was born in Cádiz, Spain. He received the Electrical Engineer degree from the Universidad Politécnica de Madrid, Madrid, Spain, in 1973 and the Ph.D. degree from the Ecole Polytechnique Fédérale de Lausanne (EPFL), Lausanne, Switzerland, in 1983.

Since 1991, he has been a Professor at EPFL where, since 2000, he has been the Head of the Laboratory of Electromagnetics and Acoustics (LEMA). He is also currently a co-Director of the College of Humanities and the Chairman of the EPFL Space Center, conducting many Swiss research projects for the European Space Agency (ESA). In 1984, he was a Visiting Research Associate with the Rochester Institute of Technology, Rochester, NY, and Syracuse University, Syracuse, NY. He has also held scientific appointments with the University of Rennes, France, the University of Nice, France, the Technical University of Denmark at Lyngby and the University of Colorado at Boulder. He has authored five chapters in books on planar antennas and circuits and over 100 peer-reviewed journal papers. His current research interests include electromagnetic theory, numerical methods, and planar antennas.

Dr. Mosig is a also a Fellow of the IEEE, the chairperson of the European COST Action on Antennas "ASSIST" (2007–2011) and a founding member and acting Chair of the European Association & Conferences on Antennas and Propagation (EurAAP and EuCAP).

Anja K. Skrivervik received the Electrical Engineering degree and the Ph.D. degree from Ecole Polytechnique Fédérale de Lausanne, in 1986 and 1992, respectively.

Previously, she worked at the University of Rennes and in the industry before returning to EPFL in 1996 as an Assistant Professor, and where she is currently a "Professeur titulair." Her teaching activities include courses on microwaves and on antennas. Her research activities include electrically small antennas, multi-frequency and ultrawideband antennas, numerical techniques for electromagnetic and microwave and millimeter wave MEMS. She is author or coauthor of more than 100 scientific publications.

Prof. Skrivervik is very active in European collaboration and European projects. She is currently the Chairperson of the Swiss URSI, the Swiss representative for COST action 297 and a member of the board of the Center for High Speed Wireless Communications of the Swedish Foundation for Strategic Research.